



1 **Quantifying the tropospheric ozone radiative effect and its temporal evolution in the satellite-era**

2 Richard J. Pope<sup>1,2</sup>, Alexandru Rap<sup>1</sup>, Matilda A. Pimlott<sup>1</sup>, Brice Barret<sup>3</sup>, Eric Le Flochmoen<sup>3</sup>, Brian J.  
3 Kerridge<sup>4,5</sup>, Richard Siddans<sup>4,5</sup>, Barry G. Latter<sup>4,5</sup>, Lucy J. Ventress<sup>4,5</sup>, Anne Boynard<sup>6,7</sup>, Christian  
4 Retscher<sup>8</sup>, Wuhu Feng<sup>1,9</sup>, Richard Rigby<sup>1,10</sup>, Sandip S. Dhomse<sup>1,2</sup>, Catherine Wespes<sup>11</sup> and Martyn P.  
5 Chipperfield<sup>1,2</sup>

6

7 *1: School of Earth and Environment, University of Leeds, Leeds, UK*

8 *2: National Centre for Earth Observation, University of Leeds, Leeds, UK*

9 *3: LAERO/OMP, Université de Toulouse, Toulouse, France*

10 *4: Remote Sensing Group, STFC Rutherford Appleton Laboratory, Chilton, UK*

11 *5: National Centre for Earth Observation, STFC Rutherford Appleton Laboratory, Chilton, UK*

12 *6: LATMOS/IPSL, Sorbonne Université, UVSQ, CNRS, Paris, 75005, France*

13 *7: SPASCI, Ramonville-Saint-Agne, 31520, France*

14 *8: ESA/ESRIN, Frascati, Italy*

15 *9: National Centre for Atmospheric Science, University of Leeds, Leeds, UK*

16 *10: Centre for Environmental Modelling and Computation, University of Leeds, Leeds, UK*

17 *11: Université libre de Bruxelles (ULB), Spectroscopy, Quantum Chemistry and Atmospheric Remote*  
18 *Sensing, Brussels, Belgium*

19

20 *Correspondence to: Richard J. Pope ([r.j.pope@leeds.ac.uk](mailto:r.j.pope@leeds.ac.uk))*

21 **Key Points:**

- 22 • Using satellite data and model simulations, we quantify the long-term (2008-2017) global  
23 average tropospheric ozone radiative effect to range between 1.21 and 1.28 W/m<sup>2</sup>.
- 24 • Satellite/modelled long-term trends in the tropospheric ozone radiative effect have  
25 remained stable (2008-2017) yielding no substantial changing influences on climate.
- 26 • Meteorological variability has been important in stabilising the global tropospheric ozone  
27 radiative effect with time.

28 **Abstract:**

29 Using state-of-the-art satellite ozone profile products, and chemical transport model, we provide an  
30 updated estimate of the tropospheric ozone radiative effect (TO<sub>3</sub>RE) and observational constraint on  
31 its variability over the decade 2008-2017. Previous studies have shown the short-term (i.e. a few  
32 years) globally weighted average TO<sub>3</sub>RE to be 1.17±0.03 W/m<sup>2</sup>, while our analysis suggests that the  
33 long-term (2008-2017) average TO<sub>3</sub>RE to be 1.21-1.28 W/m<sup>2</sup>. Over this decade, the  
34 modelled/observational TO<sub>3</sub>RE linear trends show negligible change (i.e. ±0.1%/year), so the  
35 tropospheric ozone radiative contribution to climate has remained stable with time. Two model  
36 sensitivity experiments fixing emissions and meteorology to one year (i.e. start year – 2008) show



37 that ozone precursor emissions (meteorological factors) have had limited (substantial) impacts on  
38 the long-term tendency of globally weighted average TO<sub>3</sub>RE. Here, the meteorological variability in  
39 the tropical/sub-tropical upper troposphere is dampening any tendency in TO<sub>3</sub>RE from other factors  
40 (e.g. emissions, atmospheric chemistry).

#### 41 **Plain Language Summary:**

42 Tropospheric ozone is a potent air pollutant and an important short-lived climate forcer (SLCF). It is a  
43 secondary pollutant formed through chemical reactions of precursor gases and sunlight. As a SLCF, it  
44 influences the incoming solar short-wave radiation and the outgoing long-wave radiation in the  
45 upper troposphere (approximately at altitudes of 10-15 km) where the balance between the two  
46 yields a net positive (i.e. warming) effect at the surface. The majority of previous estimates of the  
47 tropospheric ozone radiative effect (TO<sub>3</sub>RE) have been quantified from atmospheric chemistry  
48 climate model simulations. However, satellite retrievals of tropospheric ozone in recent decades  
49 have provided the opportunity to estimate these model TO<sub>3</sub>RE estimates. In this study, we utilise  
50 satellite ozone profile retrievals from the Infrared Atmospheric Sounding Interferometer (IASI), on-  
51 board the MetOp-A satellite, to derive a long-term average TO<sub>3</sub>RE estimate of 1.21-1.28 W/m<sup>2</sup>.  
52 While this builds upon previous studies (e.g. TO<sub>3</sub>RE estimates of 1.17±0.03 W/m<sup>2</sup>), the improved  
53 spatial coverage and temporal record of IASI also allows for the assessment of TO<sub>3</sub>RE variability and  
54 tendencies on a decadal scale. Here, we find negligible trends in the TO<sub>3</sub>RE (2008-2017) suggesting  
55 that the contribution of tropospheric ozone to climate, via radiative properties, remained stable  
56 over that period.

#### 57 **1. Introduction**

58 Tropospheric ozone (TO<sub>3</sub>) is a short-lived climate forcer (SLCF). It is the third most important  
59 greenhouse gas (GHG; Myhre et al., 2013) and a hazardous air pollutant with adverse impacts on  
60 human health (WHO, 2018) and the biosphere (e.g. agricultural and natural vegetation; Sitch et al.,  
61 2007). Since the pre-industrial (PI) period, anthropogenic activities have increased the atmospheric  
62 loading of ozone (O<sub>3</sub>) precursor gases, most notably nitrogen oxides (NO<sub>x</sub>) and methane (CH<sub>4</sub>),  
63 resulting in an increase in TO<sub>3</sub> of 25-50% since 1900 (Gauss et al., 2006; Lamarque et al., 2010; Young  
64 et al., 2013). The PI to present day (PD) radiative forcing (RF) from TO<sub>3</sub> is estimated to be 0.4 (0.2-  
65 0.6) Wm<sup>-2</sup> (Myhre et al., 2013; Stevenson et al., 2013) based on model simulations.

66 While models provide a valuable framework to quantify the TO<sub>3</sub> RF, observations are required to  
67 validate the models' representation of TO<sub>3</sub> and TO<sub>3</sub> RF. Observations are not available for the PI, but  
68 multiple satellite products of TO<sub>3</sub> are readily available in the PD (e.g. Richards et al., 2008; Boynard  
69 et al., 2018; Barret et al., 2020). The tropospheric ozone radiative effect (TO<sub>3</sub>RE) is defined as the  
70 radiative flux imbalance at the tropopause between incoming short-wave solar radiation and the  
71 outgoing long-wave radiation due to the presence of TO<sub>3</sub> (Rap et al., 2015). Therefore, satellite  
72 ozone profile datasets from infrared instruments, in combination with off-line ozone radiative  
73 kernels to account for vertical sensitivity (e.g. Bowman et al., (2013); Rap et al., 2015), can be used  
74 to quantify the PD TO<sub>3</sub>RE and thus provide some constraint on modelled TO<sub>3</sub>RE which is used to  
75 derive the TO<sub>3</sub>RF.

76 Several studies have previously used satellite data to derive short-term estimates of the TO<sub>3</sub>RE (i.e.  
77 from a few months of data). Joiner et al., (2009) used tropospheric column ozone (TCO<sub>3</sub>) data based  
78 on two satellite instruments: Ozone Monitoring Instrument (OMI) and Microwave Limb Sounder



79 (MLS) measurements, also known as OMI-MLS product for January and July 2005, to estimate the  
80 resultant instantaneous TO<sub>3</sub>RE at the tropopause to be 1.53 W/m<sup>2</sup>. Worden et al., (2008) used ozone  
81 profile data for 2006 from the Tropospheric Emissions Spectrometer (TES), on-board NASA's Aura  
82 satellite, to estimate the average instantaneous long-wave TO<sub>3</sub>RE at the top-of-the-atmosphere  
83 (TOA) over the oceans (45°S-45°N) to be 0.48±0.14 W/m<sup>2</sup>. Worden et al., (2011), using TES data for  
84 August 2006, estimated the instantaneous long-wave TO<sub>3</sub>RE at TOA to be 0.33 W/m<sup>2</sup>. Later, Bowman  
85 et al., (2013) also used TES data (averaged between 2005 and 2009) to constrain the simulated  
86 instantaneous long-wave TO<sub>3</sub>RE from an ensemble model average. They found that seasonally, TES  
87 long-wave TO<sub>3</sub>RE peaks in northern Africa/Mediterranean/Middle East in June-July-August over 1.0  
88 W/m<sup>2</sup> with minimum values (0.0-0.2 W/m<sup>2</sup>) over the winter-time high-latitudes. Overall, the  
89 ensemble average long-wave TO<sub>3</sub>RE low bias was 0.12 W/m<sup>2</sup>. Doniki et al., (2015) took this further  
90 by calculating the instantaneous long-wave TO<sub>3</sub>RE from the Infrared Atmospheric Sounding  
91 Interferometer (IASI), though using a small subset of the data, and found estimates from Worden et  
92 al., (2008), using TES, had a low bias of ~25%. Rap et al., (2015) also used TES satellite ozone profile  
93 observations (2005-2008) in combination with the TOMCAT chemical transport model (CTM) and  
94 provided the first robust satellite constraint on annual globally weighted resultant TO<sub>3</sub>RE (after  
95 stratospheric temperature adjustment) with a range of 1.17±0.03 W/m<sup>2</sup>.

96 Following the methodology adopted in Rap et al. (2015), we exploit satellite ozone profile data from  
97 IASI, on the MetOp-A satellite, which has a long-term record and substantial spatial coverage, in  
98 combination with the TOMCT CTM, to improve the TO<sub>3</sub>RE estimate and investigate its long-term  
99 variability and implications for climate. The satellite data, radiation model and CTM used are  
100 discussed in Section 2, our results are presented in Section 3 and Section 4 summarises our  
101 conclusions.

## 102 2. Observations and Model

### 103 2.1. Satellite Observations

104 IASI is a Michelson interferometer with a nadir-viewing spectral range between 645 and 2760 cm<sup>-1</sup>  
105 with spectral sampling of 0.25 cm<sup>-1</sup> (Illingworth et al., 2011). It measures simultaneously in four fields  
106 of view (FOV, each circular at nadir with a diameter of 12 km) in a 50 x 50km square which are  
107 scanned across track to sample a 2200 km-wide swath (Clerbaux et al., 2009). IASI, on Eumetsat's  
108 MetOp-A satellite, is in a sun-synchronous polar orbit with equator crossing local times of 9.30 (day)  
109 and 21.30 (night).

110 The three IASI products we use in this study are the IASI-FORLI product (vn 20151001, IASI-FORLI,  
111 2020; Boynard et al., 2018; Wespes et al., 2018), the IASI-SOFRID product (vn 3.5, IASI-SOFRID, 2022;  
112 Barret et al., 2020) and the RAL IASI-IMS product (IASI-IMS, 2022; Pope et al., 2021; Pimlott et al.  
113 ,2022) between 2008 and 2017 (i.e. period of consistent data coverage for all the IASI products). All  
114 three products use an optimal estimation method (OEM, Rogers, 2000) to retrieve ozone. Both IASI-  
115 SOFRID and IASI-IMS use the RTTOV radiative transfer model (Saunders et al. 1999), while the IASI-  
116 FORLI product uses look-up tables to speed up its radiative transfer calculations (Hurtmans et al.,  
117 2012). Meteorological inputs (pressure, water vapour, temperature and clouds) for IASI-FORLI come  
118 from Eumetsat level-2 data, while IASI-SOFRID uses ECMWF operational analyses and IASI-IMS uses  
119 ECMWF surface pressures and co-retrieves other meteorological and surface variables. For the  
120 ozone apriori, IASI-FORLI and IASI-IMS use the ozone climatology of McPeters et al., (2007), while  
121 IASI-SOFRID uses the dynamical ozone climatology described in Sofieva et al., (2014).



122 The IASI-FORLI level-2 data are filtered for a geometric cloud fraction  $< 0.2$ , degrees of freedom  $> 2.0$ ,  
123  $O_3$  values  $> 0.0$ , solar zenith angle  $< 80.0^\circ$  and the surface to 450 hPa sub-column  $O_3$  / total column  
124  $O_3 < 0.085$ . The IASI-SOFRID data were provided on a  $1.0^\circ \times 1.0^\circ$  horizontal grid (i.e. level-3 product,  
125 but daily temporal resolution – we used daytime retrievals only) with filtering already applied as in  
126 Barret et al., (2020). Here, only  $O_3$  values  $> 0.0$  were used. For IASI-IMS level-2, the data are filtered  
127 for a geometric cloud fraction  $< 0.5$ ,  $O_3$  values  $> 0.0$ , solar zenith angle  $< 80.0^\circ$  and a cost function  $<$   
128  $1000.0$ . However, for IASI-IMS, we relaxed the geometric cloud fraction threshold to  $0.5$  as it retains  
129 more data as the data product in this study has only been processed for 1 in 10 days and 1 in 4  
130 pixels.

## 131 2.2. Ozonesondes

132 Despite the three IASI ozone profile products using the same radiance data, the three retrieval  
133 schemes produced systematic differences between the products in the long-term  $TCO_3$  average (e.g.  
134 **Figures S2 and S3** from the **Supporting Information (SI)**). Though, the spatial structure in the three  
135 products compares well. Therefore, to harmonise the three IASI  $TCO_3$  data sets (i.e. absolute values  
136 but not long-term variability) we use ozonesonde data from the World Ozone and Ultraviolet  
137 Radiation Data Centre (WOUDC; WOUDC, 2023), the Southern Hemisphere Additional Ozonesondes  
138 (SHADOZ; SHADOZ, 2023) project and the Global Monitoring Laboratory, National Oceanic and  
139 Atmospheric Administration (NOAA; NOAA, 2023). Here,  $O_3$  measurements were rejected if the  $O_3$  or  
140 pressure values were unphysical (i.e.  $< 0.0$ ), if the  $O_3$  partial pressure  $> 2000.0$  mPa or the  $O_3$  value  
141 was set to 99.9, and whole ozonesonde profiles were rejected if least 50% of the measurements did  
142 not meet these criteria. These criteria are similar to those applied by Keppins et al., (2018) and  
143 Hubert et al., (2016). To allow for direct like-for-like comparisons between the two quantities,  
144 accounting for the vertical sensitivity of the satellite, the instrument averaging kernels (AKs) are  
145 applied the ozonesonde profiles as:

$$146 \quad \mathit{sonde}_{AK} = AK \cdot (\mathit{sonde}_{int} - \mathit{apr}) + \mathit{apr} \quad (1)$$

147 where  $\mathit{sonde}_{AK}$  is the modified ozonesonde sub-column profile,  $AK$  is the averaging kernel matrix,  
148  $\mathit{sonde}_{int}$  is the ozonesonde sub-column profile interpolated on the satellite pressure grid and  $\mathit{apr}$  is  
149 the a priori for the satellite retrieval. For the application of the AKs to the ozonesonde profiles, the  
150 full ozone profile is required which is not available from the ozonesondes (i.e. mid-stratosphere and  
151 above). Therefore, the ozonesonde profile above its minimum pressure level is extended using the  
152 a priori profile from the corresponding satellite product. The profile is smoothed vertically across the  
153 joining pressure level to avoid a profile discontinuity.

154 Once the ozonesondes had been co-located with the satellite data (i.e. within 6-hours and 500 km)  
155 and the AKs applied, the two datasets were compared across the full 2008-2017 period. We typically  
156 find a global annual  $TCO_3$  systematic bias of 14.9%, 2.7% and 17.4% for IASI-FORLI, IASI-SOFRID and  
157 IASI-IMS, respectively, which is consistent with Boynard et al., (2018), Barret et al., (2020) and  
158 Pimlott et al., (2022). Here, we generated annual-latitude ( $30^\circ$  bins) bias correction factors (BCF)  
159 which were applied to the gridded satellite records (see **SI-2**) to harmonise the retrieved  $TCO_3$  (i.e.  
160 remove the systematic errors) and scale the derived  $TO_3RE$ . This is an important exercise as it  
161 provides a more accurate absolute range in satellite retrieved  $TCO_3$  (and the ozone values used to  
162 derive the  $TO_3RE$ ) but as the ozonesondes generally have poor spatial coverage, the global coverage  
163 and spatial distribution of the satellite data is critical in our analysis. Note, that as a climatology was



164 used, the systematic biases in the satellite records were affected but their long-term temporal  
165 variability retained.

### 166 2.3. TOMCAT

167 In this study, we use the 3D global chemical transport model TOMCAT (Chipperfield, 2006), which  
168 has a detailed tropospheric chemistry scheme including 229 gas-phase reactions and 82 advected  
169 tracers (Monks et al., 2017). Model heterogeneous chemistry uses size-resolved aerosol from the  
170 GLOMAP module (Mann et al., 2010). The model was run between 2008 and 2017 at a  $2.8^{\circ} \times 2.8^{\circ}$   
171 spatial resolution with 31 vertical levels between the surface and 10hPa. The model is forced by  
172 meteorological reanalyses (ERA-Interim) from the European Centre for Medium-Range Weather  
173 Forecasts (ECMWF; Dee et al., 2011) including reanalysis cloud fields and mass fluxes (e.g. as in  
174 Rowlinson et al., 2020, Pimlott et al., 2022). Annually varying anthropogenic emissions come from  
175 the Coupled Model Intercomparison Project Phase 6 (CMIP6, Feng et al., 2020). Climatological  
176 biogenic emissions are from the Chemistry-Climate Model Initiative (CCMI; Morgenstern et al., 2017)  
177 but isoprene and monoterpene emissions are annually varying from the Joint UK Land Environment  
178 Simulator (JULES, Pacifico et al., 2011) within the free-running UK Earth System Model (UKESM,  
179 Sellar et al., 2019). Other natural emissions come from the Precursors of Ozone and their Effects in  
180 the Troposphere (POET, Olivier et al., 2003) and biomass burning emissions from the Global Fire  
181 Emissions Database (GFED) version 4 (van der Werf et al., 2017). For methane ( $\text{CH}_4$ ), the model  
182 tracer is scaled to the annually varying global averaged surface  $\text{CH}_4$  value from NOAA (Dlugokencky,  
183 2020). The model was spun up for 1-year (2007) and the model tracers output daily at 09:30 local  
184 time (LT) globally to match the MetOp-A daytime overpass time. When comparing with IASI, the  
185 satellite AKs are applied to the TOMCAT vertical ozone profiles in the same way as the ozonesondes  
186 (i.e. **Equation 1**). Here, the TOMCAT ozone profile (already temporally co-located) is co-located from  
187 the model grid box the retrieval sits in. To investigate the importance of emissions and meteorology  
188 on  $\text{TO}_3$  and  $\text{TO}_3\text{RE}$ , two sensitivity experiments were run between 2008 and 2017 using repeating  
189 emissions and meteorology for 2008 (i.e. start of the time-series) annually in the model simulation  
190 over the time period.

### 191 2.4. Radiative Transfer Model and Kernel

192 The  $\text{TO}_3\text{RE}$  was calculated using the SOCRATES off-line radiative transfer model (Edwards and Slingo,  
193 1996) in combination with TOMCAT and the three IASI ozone products. SOCRATES has six bands in  
194 the short-wave and nine in the long-wave. To account for stratospheric temperature adjustments,  
195 Rap et al., (2015) used the dynamical heating approximation (Fels et al., 1980). This involved  
196 accounting for changes in the stratospheric heating rate determined from the model due to the  $\text{O}_3$   
197 perturbation, which were applied to the temperature field, with the model run iteratively until  
198 stratospheric temperatures reached equilibrium (Rap et al., 2015). This approach of using the  
199 SOCRATES off-line radiative kernel with output from model simulations to derive the  $\text{TO}_3$  radiative  
200 effect has been used in several studies e.g. Rap et al., (2015), Scott et al., (2018), Iglesias-Suarez et  
201 al. (2018) and Rowlinson et al., (2020).

202 To derive the satellite  $\text{TO}_3\text{RE}$ , the annual average IASI 3D ozone field is multiplied by the off-line  
203 radiative kernel (grid box by grid box) and then summed from the surface to the tropopause  
204 pressure. Here, the IASI ozone data is mapped onto the spatial resolution of the radiative kernel and  
205 then interpolated vertically onto its pressure grid. The equation for each grid box is:



$$TO_3RE = \sum_{i=surf}^{trop} RK_i \times O_{3i} \times dp_i/100 \quad (2)$$

207 where  $TO_3RE$  is the tropospheric ozone radiative effect ( $W/m^2$ ),  $RK$  is the radiative kernel  
208 ( $W/m^2/ppbv/100$  hPa),  $O_3$  is the satellite ozone grid box value (ppbv),  $dp$  is the pressure difference  
209 between vertical levels (hPa) and  $i$  is the grid box index between the surface pressure level and the  
210 tropopause pressure. The tropopause pressure is based on the World Meteorological Organisation  
211 (WMO) definition of “the lowest level at which the temperature lapse rate decreases to 2 K/km or  
212 less” (Bethan et al., 1996).

### 213 3. Results

#### 214 3.1. Tropospheric Ozone Radiative Effect

215 **Figure 1** shows the IASI derived  $TCO_3$ ,  $TO_3RE$  and normalised  $TO_3RE$  ( $NTO_3RE$ , i.e. the  $TO_3RE$  divided  
216 by its  $TCO_3$  as in Rap et al., (2015)). For the  $TCO_3$ , all three harmonised IASI products have good  
217 spatial agreement in the long-term (2008-2017) average with a background north-south hemisphere  
218 gradient of approximately 30.0-40.0 to 15.0-25.0 DU. Peak  $TCO_3$  (>40.0 DU) occurs over East Asia,  
219 the Middle East and ozone outflow from central Africa (e.g. from lightning and biomass burning  
220 precursor gases (Moxim & Levy, 2000)). The global average  $TCO_3$  values for IASI-FORLI, IASI-SOFRID  
221 and IASI-IMS are 32.6 DU, 29.9 DU and 29.9 DU, respectively (**Figure 1 left column**).

222 When the  $TO_3RE$  is calculated (**Figure 1 middle column**), peak values occur over the sub-tropics,  
223 Africa and Australia ranging between approximately 2.0 and 2.5  $W/m^2$  consistently for each IASI  
224 product. The minimum values are in the high latitudes ranging between 0.0 and 0.8  $W/m^2$  where  $TO_3$   
225 appears to have limited impact on the  $TO_3RE$ . The bottom panel of **Figure 1** supports this as the  
226 zonally average profiles, weighted by the cosine of degrees latitude, show that  $TCO_3$  is near-zero in  
227 the high-latitudes, approximately 15.0-20.0 DU in the mid-latitudes, peaking at 28.0-33.0 DU in the  
228 sub-tropics and then decreasing by several DU at the tropics. The corresponding  $TO_3RE$  profiles  
229 follow a similar pattern with near-zero values at the high-latitudes, approximately 0.5-1.0  $W/m^2$  in  
230 the mid-latitudes, peak at 1.5  $W/m^2$  in the sub-tropics and then decrease to 1.1-1.2  $W/m^2$  in the  
231 tropics. Therefore, the sub-tropics have the largest contribution to the global  $TO_3RE$ . The global  
232 weighted  $TO_3RE$  averages for IASI-FORLI, IASI-SOFRID and IASI-IMS are 1.23, 1.21 and 1.21  $W/m^2$ ,  
233 respectively.

234 The  $NTO_3RE$  (**Figure 1 right column**) provides an estimate of where the  $TO_3RE$  is most sensitive to  
235 changes in  $TCO_3$  (i.e. the unit of  $TO_3RE$  per unit of  $TCO_3$ ). Peak  $NTO_3RE$  (>45.0  $mW/m^2/DU$ ) occurs in  
236 similar locations to the peak  $TO_3RE$  (e.g. sub-tropics, Africa and Australia), while the minimum values  
237 (10.0-20.0  $mW/m^2/DU$ ) occur in the high-latitudes. However, while the South Pacific  $TCO_3$  values  
238 (23.0-30.0) are lower than other ocean regions (e.g. >30.0 DU), the  $NTO_3RE$  values are of similar  
239 magnitude (approximately 50.0  $mW/m^2/DU$ ). Therefore, while the sub-tropical/mid-latitude oceans  
240 have reasonable large  $TCO_3$  and  $TO_3RE$  values, the South Pacific is more effective at contributing to  
241 the  $TO_3RE$ , despite its lower  $TCO_3$  values (i.e. more positive radiative effect per unit of  $TO_3$ ).

242 Overall, the global weighted average  $NTO_3RE$  is 37.78, 40.43 and 40.60  $mW/m^2/DU$  for IASI-FORLI,  
243 IASI-SORID and IASI-IMS, respectively. Based on the AKs, the tropospheric degrees of freedom of  
244 signal (DOFS, between the surface and 170 hPa – approximate tropopause) is approximately 1.0 for  
245 all three IASI products (not shown here). However, it is likely that differences in the IASI ozone  
246 profiles are driving the contrasting globally averaged  $NTO_3RE$  values. As the IASI-FORLI  $NTO_3RE$  is  
247 lower, while having the highest global average  $TCO_3$  and  $TO_3RE$ , it suggests that IASI-FORLI has more



248 TO<sub>3</sub> in the mid-troposphere where the radiative kernel has less sensitivity. Further to this, as the IASI  
249 ozone products only have approximately 1.0 DOFS, the harmonisation of the products using the  
250 ozonesondes can only be done on a tropospheric column level and thus the scaling of the satellite  
251 derived TO<sub>3</sub>RE (i.e. even though the upper troposphere is the most sensitive region to ozone  
252 radiative properties, the scaling of the TO<sub>3</sub>RE is applied based on the satellite-ozonesonde TCO<sub>3</sub>  
253 relative differences).

254 TOMCAT allows for a further quantification of the TO<sub>3</sub>RE in the satellite-era and the ability to run  
255 sensitivity experiments to explore important processes. Therefore, the TOMCAT equivalent metrics  
256 from **Figure 1** are presented in **Figure 2**. Evaluation of the model using the IASI products and  
257 ozonesondes (see **SI-2, Figure S3 & S4**) shows the model generally captures the TCO<sub>3</sub> spatial pattern  
258 and absolute values. In the tropics (mid/high-latitudes), the model underestimates (overestimates)  
259 by approximately 10-20% on average. These biases are comparable with other modelling studies  
260 evaluating models against satellite TO<sub>3</sub> observations (e.g. Archibald et al., 2020; Monks et al., 2017;  
261 Nassar et al., 2009; Young et al., 2013), indicating that TOMCAT is a suitable modelling framework in  
262 this study.

263 The globally mean TCO<sub>3</sub> from TOMCAT (2008-2017) with the three sets of AKs applied (**Figure 2 left**  
264 **column**) ranges between 31.6 and 32.5 DU, so it slightly larger than the IASI data sets in **Figure 1**.  
265 When translated into TO<sub>3</sub>RE, the peak values from TOMCAT (with AKs applied) ranges between 2.0  
266 and >2.5 W/m<sup>2</sup> over Africa, Australia and the sub-tropics. The globally weighted TO<sub>3</sub>RE for TOMCAT  
267 with the IASI-FORLI and IASI-SOFRID AKs applied is 1.28 W/m<sup>2</sup> and thus moderately higher than IASI  
268 (1.21-1.23 W/m<sup>2</sup>) but comparable overall. However, the globally weighted TO<sub>3</sub>RE for TOMCAT with  
269 IASI-IMS AKs applied is larger at 1.34 W/m<sup>2</sup>. As TOMCAT has a positive TCO<sub>3</sub> bias with the  
270 observations in the sub-tropics, where the TO<sub>3</sub>RE influence is most pronounced, this probably  
271 explains the larger model TO<sub>3</sub>RE values. In the bottom panel of **Figure 2**, the zonal profiles (weighted  
272 by cosine of degree latitude) for TCO<sub>3</sub> (TO<sub>3</sub>RE) are consistent with IASI as high-latitude values are  
273 near-zero, mid-latitude values range between 10.0 and 20.0 DU (0.5 to 1.0 W/m<sup>2</sup>) and sub-tropical  
274 values range between 30.0 and 38.0 DU (1.5 and 1.7 W/m<sup>2</sup>). There is a decrease to approximately  
275 25.0 DU (1.0-1.3 W/m<sup>2</sup>) in the tropics. In terms of the NTO<sub>3</sub>RE, the TOMCAT (with AKs applied) global  
276 weighted values range between 39.4 and 42.4 mW/m<sup>2</sup>/DU, which is similar to IASI. The peak NTO<sub>3</sub>RE  
277 values are over the oceans (50.0-60.0 mW/m<sup>2</sup>/DU) and over Africa/Australia (>60.0 mW/m<sup>2</sup>/DU).  
278 Like for IASI, the TCO<sub>3</sub> values over the South Pacific are lower than the other ocean values but the  
279 NTO<sub>3</sub>RE values are similar, again showing that despite the lower TO<sub>3</sub>, the South Pacific region is  
280 important for the global TO<sub>3</sub>RE given its greater sensitivity (i.e. more radiative effect per unit of TO<sub>3</sub>).

### 281 **3.2. Temporal Evolution of the Tropospheric Ozone Radiative Effect**

282 As IASI has daily global coverage (Clerbaux et al., 2009), we are able to derive annual average 3D  
283 ozone fields between 2008 and 2017, thus providing the first assessment of temporal variability and  
284 tendency in satellite derived TO<sub>3</sub>RE. **Figure 3** shows the annual TO<sub>3</sub>RE time series for all three IASI  
285 products. First thing to note, is that the Eumetsat meteorological data used to retrieve ozone for the  
286 IASI-FORLI product is subject to inhomogeneities (Boynard et al., 2018; Wespes et al., 2018). As a  
287 result, we include long-term analysis of the IASI-FORLI data for the full time period (2008-2017) and  
288 then a sub-time period (2011-2017) given the large inhomogeneity in September 2010 reported by  
289 Boynard et al., (2018) and Wespes et al., (2018). Here, we can derive the TO<sub>3</sub>RE to quantify the  
290 absolute values (e.g. are they generally similar year to year) and how they compare between



291 products over the two time periods. In the near future, a new consistent IASI-FORLI ozone climate  
292 data record will be available using homogeneous level-2 Eumetsat meteorological data.

293 For IASI-SOFRID and IASI-IMS, the annual TO<sub>3</sub>RE values range between 1.19 and 1.24 W/m<sup>2</sup> across  
294 the 2008-2017 time period. IASI-FORLI has somewhat larger values at the start of the record (1.26-  
295 1.28 W/m<sup>2</sup>) before tending to that of IASI-SOFRID/IASI-IMS from 2011 onwards. Correlations  
296 (squared) in the annual TO<sub>3</sub>RE time-series between IASI-FORLI and IASI-SOFRID (IASI-IMS) are poor at  
297 R<sup>2</sup>=0.148 (R<sup>2</sup>=0.132). However, IASI-SOFRID and IASI-IMS have a much stronger agreement with  
298 R<sup>2</sup>=0.591 (significant at the 95<sup>th</sup> confidence level, CL95%) sharing nearly 60% of the temporal  
299 variability. We also calculate the coefficient of variation (CoV, i.e., time series standard deviation  
300 divided by its mean) to assess the inter-annual variability. For IASI-SOFRID and IASI-IMS, this is 1.1%,  
301 but for IASI-FORLI it is 2.5%. Therefore, there is more year-to-year variability in the IASI-FORLI TO<sub>3</sub>RE  
302 record. However, when focussing on IASI-FORLI data for 2011-2017, the CoV drops to 1.2% in-line  
303 with IASI-SOFRID and IASI-IMS. The correlation (squared) values are now R<sup>2</sup><sub>FORLI-SOFRID</sub>=0.496  
304 (significant at the CL95%) and R<sup>2</sup><sub>FORLI-IMS</sub>=0.137, which shows improved agreement between IASI-  
305 FORLI and IASI-SOFRID, but slightly surprisingly not with IASI-IMS. Using ordinary least squares fit  
306 regression, IASI-FORLI, IASI-SOFRID and IASI-IMS have global average weighed TO<sub>3</sub>RE linear trends  
307 of -0.6%/year (CL95%), 0.0%/year (non-significant) and -0.1%/year (non-significant). As the IASI-  
308 FORLI product has known inhomogeneities (hence the larger CoV), the insignificant IASI-SOFRID and  
309 IASI-IMS trends are more robust. This is supported by IASI-FORLI when only considering 2011-2017  
310 with an insignificant linear trend of -0.2%/year. Therefore, this suggests negligible change in the  
311 contribution of TO<sub>3</sub> to the tropospheric radiative effect and thus climate over the recent past (i.e.  
312 2008-2017).

313 TOMCAT global average weighed TO<sub>3</sub>RE (without AKs applied) ranges between 1.24 and 1.29 W/m<sup>2</sup>  
314 between 2008 and 2017. The CoV is 1.5% for TOMCAT, so it is larger than both IASI-SOFRID and IASI-  
315 IMS. When the IASI AKs are applied to TOMCAT, there is a substantial shift in the modelled absolute  
316 TO<sub>3</sub>RE values. TOMCAT with IASI-SOFRID and IASI-FORLI AKs applied ranged between 1.28 and 1.30  
317 W/m<sup>2</sup>. And for TOMCAT with the IASI-IMS AKs applied, the TO<sub>3</sub>RE values peak at 1.33 to 1.34 W/m<sup>2</sup>  
318 between 2008 and 2017. As well as the increase in TO<sub>3</sub>RE values, the application of the AKs squashes  
319 the TOMCAT inter-annual variability with corresponding CoV values between 0.4 and 0.6%, which is  
320 smaller than the original CoV of 1.5%. Interestingly, without the application of the AKs, the TOMCAT  
321 TO<sub>3</sub>RE time-series has similar temporal variability (e.g. peaks in 2008, 2010 and 2017 and troughs in  
322 2009 and 2014). Overall, all the TOMCAT TO<sub>3</sub>RE time-series (with and without AKs applied have  
323 insignificant linear trends ranging between -0.1%/year and 0.1%/year. Therefore, even with the  
324 influence of the IASI AKs on the TOMCAT TO<sub>3</sub>RE time-series, there appears to be a negligible trend in  
325 the modelled TO<sub>3</sub>RE, supporting that of the IASI records. As a result, between 2008 and 2017, there  
326 has been limited change in TO<sub>3</sub> and TO<sub>3</sub>RE, thus the impact of TO<sub>3</sub> on climate has remained stable.

327 To investigate the importance of emissions and meteorology on the long-term TO<sub>3</sub>RE trends,  
328 TOMCAT was run using repeating emissions and repeating meteorology for 2008 (i.e. start of the  
329 time-series) in two sensitivity experiments for the full time-period. Here, we find that in absolute  
330 terms, using fixed emissions reduces the TO<sub>3</sub> burden and the TO<sub>3</sub>RE as the time-series drops to 1.22  
331 to 1.28 W/m<sup>2</sup> (i.e. minima in 2014 and 2015 more pronounced). However, the trend in TO<sub>3</sub>RE (-  
332 0.2%/year) remains insignificant and that emissions are only moderately important in driving long-  
333 term tendencies in TO<sub>3</sub>RE. On the other hand, meteorological factors, while not dramatically altering  
334 the absolute simulated TO<sub>3</sub>RE values, are more important as fixing the meteorology yields a steady





335 and significant increase (0.3%/year). Thus, without year-to-year variability in meteorology, temporal  
336 variability in TO<sub>3</sub> would likely have a more substantial impact on the present day climate.

337 **Figure 4** shows the horizontal and vertical impact of the two sensitivity experiments on TOMCAT O<sub>3</sub>  
338 radiative effect (note the different colour bar scales). Consistent with **Figures 1** and **2**, the TOMCAT  
339 control TO<sub>3</sub>RE has peak values (>2.50 W/m<sup>2</sup>) over northern Africa and throughout the sub-tropics  
340 (approximately 2.0 W/m<sup>2</sup>, **Figure 4a**). Vertically, the TOMCAT peak ozone radiative effect (>0.25  
341 W/m<sup>2</sup>) is in the upper troposphere (**Figure 4b**) with the largest impact in the sub-tropics of both  
342 hemispheres (500-200 hPa). Similar values extend through the hemispheric mid-latitudes but in a  
343 smaller pressure range (400-300 hPa). As shown in **Figure 3**, the fixed meteorological run imposes a  
344 significant TO<sub>3</sub>RE trend on the modelled tendency between 2008 and 2017. From **Figure 4c**, the  
345 difference between the fixed meteorology and control runs shows mainly positive TO<sub>3</sub>RE differences  
346 of 0.1 to >0.2 W/m<sup>2</sup> throughout the tropics and sub-tropics, though there is considerable spatial  
347 variation due to changes in the global circulation. In the high and mid-latitudes, there are smaller  
348 scale negative differences ranging between -0.1 and 0.0 W/m<sup>2</sup> (though some differences up to -0.15  
349 W/m<sup>2</sup> in the sub-tropical Pacific). In the upper troposphere (**Figure 4d**), the zonal average O<sub>3</sub>  
350 radiative effect is consistent with positive differences of up to 0.02 W/m<sup>2</sup> at approximately 200 hPa  
351 in the tropics and sub-tropics. The positive differences (approximately 0.01 W/m<sup>2</sup>) filter down to 600  
352 hPa in the same latitudinal range. In the mid-latitudes, the peak negative differences are  
353 approximately -0.02 to -0.015 W/m<sup>2</sup> at 300 hPa, with a reach down to 500 hPa at -0.005 W/m<sup>2</sup>.  
354 Overall, as shown in **Figure 3**, the fixed meteorology run increases the global average TO<sub>3</sub>RE. While  
355 this could be a specific signal related to the 2008 meteorology (i.e. it is conducive to TO<sub>3</sub> formation),  
356 it clearly shows that the upper tropospheric tropical and sub-tropical regions predominantly control  
357 the global TO<sub>3</sub>RE average and its temporal variability (i.e. the region where the meteorological inter-  
358 annual variability is buffering underlying increases in TO<sub>3</sub>RE). With fixed emissions, there is a general  
359 increase (decrease) in TO<sub>3</sub>RE in the tropics/sub-tropics (northern mid-latitudes) by 0.02 (-0.02)  
360 W/m<sup>2</sup>. However, over tropical Asia, Indonesia and Australia, the decrease in TO<sub>3</sub>RE is more  
361 substantial at -0.05 to -0.04 W/m<sup>2</sup> (**Figure 4e**). Vertically, there are decreases (increases) in the O<sub>3</sub>  
362 radiative effect of -0.005 (0.003) W/m<sup>2</sup> in the tropics/sub-tropics (northern mid-latitudes) between  
363 600 and 200 (800 and 400) hPa (**Figure 4f**). Overall, the meteorological variability, in comparison to  
364 the long-term emission changes in O<sub>3</sub> precursor gases, has substantially more influence on the inter-  
365 annual variability of the global TO<sub>3</sub>RE over this decade.

#### 366 4. Conclusions

367 By using state-of-the-art satellite ozone profile retrievals from the Infrared Atmospheric Sounding  
368 Interferometer (IASI), on-board MetOp-A, in combination with the TOMCAT chemical transport  
369 model (CTM), we provide an updated estimate of the tropospheric ozone radiative effect (TO<sub>3</sub>RE)  
370 and provide the first observational constraint on its variability over the decade 2008-2017. Building  
371 upon the previous study of Rap et al., (2015), who quantified the globally weighed average TO<sub>3</sub>RE to  
372 be 1.17±0.03 W/m<sup>2</sup> (based on data between 2005 and 2008), we find the long-term average TO<sub>3</sub>RE,  
373 between 2008 and 2017, to range from 1.21 and 1.28 W/m<sup>2</sup>. Secondly, neither the modelled, nor the  
374 observed TO<sub>3</sub>RE suggest any substantial change during this period. Therefore, the tropospheric  
375 ozone contribution to climate, through its infrared radiative properties, has remained stable with  
376 time during 2008-2017. Investigations of the importance of ozone precursor emissions and  
377 meteorology, through targeted sensitivity experiments repeating emissions and meteorology for  
378 2008 (i.e. year at start of time-series), suggest that emissions have a limited impact on the globally



379 weighted average TO<sub>3</sub>RE. Meanwhile, fixing the meteorology to a specific year (i.e. 2008) introduces  
380 a significant positive trend in global TO<sub>3</sub>RE, indicating that the meteorological variability in the  
381 tropical/sub-tropical upper troposphere has been important in stabilising the tropospheric ozone  
382 contribution to climate, via radiative properties, in the recent past (i.e. satellite-era).

### 383 **Acknowledgements**

384 This work was funded by the UK Natural Environment Research Council (NERC) by providing funding  
385 for the National Centre for Earth Observation (NCEO, award reference NE/R016518/1) and funding  
386 from the European Space Agency (ESA) Climate Change Initiative (CCI) post-doctoral fellowship  
387 scheme (award reference 4000137140). The IASI-SOFRID research was conducted at LAERO with  
388 some financial support from the CNES French spatial agency (TOSCA–IASI project).

### 389 **Data Availability**

390 The IASI-FORLI and IASI-SOFRID data can be obtained from <https://iasi.aeris-data.fr/O3> and  
391 <https://iasi-sofrid.sedoo.fr/>. The IASI-IMS data is available via the NERC Centre for Environmental  
392 Data Analysis (CEDA) Jasmin platform subject to data requests. However, the IASI-IMS data and  
393 TOMCAT simulations used in this study are available from  
394 <https://homepages.see.leeds.ac.uk/~earrijo/to3re/>. The ozonesonde data for WOUDC, SHADOZ and  
395 NOAA is available from <https://woudc.org/>, <https://tropo.gsfc.nasa.gov/shadoz/> and  
396 <https://gml.noaa.gov/ozwv/ozsondes/>.

### 397 **Author Contributions**

398 RJP conceptualised, planned and undertook the research study. AR provided the SOCRATES radiative  
399 kernel. BB, ELF, BJK, RS, BGL, LJV, AB and CW provided the IASI ozone data and advice on using the  
400 products. MAP performed the TOMCAT model simulations with support from MPC and WF. CR  
401 provided advice and help during RP's ESA CCI fellowship. RJP prepared the manuscript with  
402 contributions from all co-authors.

### 403 **Conflicts of Interest**

404 The authors declare no conflicts of interest.

### 405 **References**

- 406 Archibald, A.T., O'Connor, F.M., Abraham, N.A., et al. 2020. Description and evaluation of the UKCA  
407 stratosphere–troposphere chemistry scheme (StratTrop vn 1.0) implemented in UKESM1.  
408 *Geoscientific Model Development*, **13**, 1223–1266, doi: 10.5194/gmd-13-1223-2020.
- 409 Barret, B., Le Flochmoen, E., Sauvage, B., et al. 2011. The detection of post-monsoon tropospheric  
410 ozone variability over south Asia using IASI data. *Atmospheric Chemistry and Physics*, **11**, 9533–9548,  
411 doi: 10.5194/acp-11-9533-2011.
- 412 Barret, B., Emili, E., Le Flochmoen, E. 2020. A tropopause-related climatological a priori profile for  
413 IASI-SOFRID ozone retrievals: improvements and validation. *Atmospheric Measurement Techniques*,  
414 **13**, 5237–5257, doi: 10.5194/amt-13-5237-2020.
- 415 Bethan, S., Vaughan, G. and Reid, S.J. 1996. A comparison of ozone and thermal tropopause heights  
416 and the impact of tropopause definition on quantifying the ozone content of the troposphere.  
417 *Journal of Quantitative Spectroscopy and Radiative Transfer*, **122**: 929–944, doi:  
418 10.1002/qj.49712253207.



- 419 Bowman, K.W., Shindell, D.T., Worden, H.M., et al. 2013. Evaluation of ACCMIP outgoing longwave  
420 radiation from tropospheric ozone using TES satellite observations. *Atmospheric Chemistry and*  
421 *Physics*, **13**, 4057–4072, doi: 10.5194/acp-13-4057-2013.
- 422 Boynard, A., Hurtmans, D., Garane, K., et al. 2018. Validation of the IASI FORLI/EUMETSAT ozone  
423 products using satellite (GOME-2), ground-based (Brewer-Dobson, SAOZ, FTIR) and ozonesonde  
424 measurements. *Atmospheric Measurement Techniques*, **11** (9), doi: 10.5194/amt-11-5125-2018.
- 425 Chipperfield, M.P. 2006. New version of the TOMCAT/SLIMCAT off-line chemistry transport model:  
426 Intercomparison of stratospheric trace experiments. *Quarterly Journal of the Royal Meteorological*  
427 *Society*, **132**, 1179–1203, doi:10.1256/qj.05.5.
- 428 Clerbaux, A., Boynard, A., Clarisse, L., et al. 2009. Monitoring of atmospheric composition using the  
429 thermal infrared IASI/MetOp sounder. *Atmospheric Chemistry and Physics*, **9**, 6041–6054, doi:  
430 10.5194/acp-9-6041-2009.
- 431 Dee, D.P., Uppala, S.M., Simmons, A.J., et al.: The ERA-Interim reanalysis: Configuration and  
432 performance of the data assimilation system, *Quarterly Journal of the Royal Meteorological Society*,  
433 **137** (656), 553–597, doi:10.1002/qj.828, 2011.
- 434 Dlugokencky, E. 2020. NOAA Global Monitoring Laboratory–Trends in Atmospheric Methane,  
435 Available at: [https://gml.noaa.gov/ccgg/trends\\_ch4/](https://gml.noaa.gov/ccgg/trends_ch4/) (last accessed 23/01/2023).
- 436 Doniki, S., Hurtmans, D., Clarisse, et al. 2015. Instantaneous longwave radiative impact of ozone: an  
437 application on IASI/MetOp observations, *Atmospheric Chemistry and Physics*, **15**, 12971–12987,  
438 doi:10.5194/acp-15-12971-2015.
- 439 Edwards, J.M and Slingo, A. 1996. Studies with a flexible new radiation code. I: Choosing a  
440 configuration for a large-scale model. *Quarterly Journal of the Royal Meteorological Society*, **122**,  
441 689–719, doi:10.1002/qj.49712253107.
- 442 Fels, S.B., Mahlman, J.D., Schwarzkopf, M.D., et al. 1980. Stratospheric Sensitivity to Perturbations in  
443 Ozone and Carbon Dioxide: Radiative and Dynamical Response. *Journal of Atmospheric Science*, **37**,  
444 2265–2297, doi: 10.1175/1520-0469(1980)037<2265:Sstpio>2.0.Co;2.
- 445 Feng, L., Smith, S. J., Braun, C., et al. 2020. The generation of gridded emissions data for CMIP6.  
446 *Geoscientific Model Development*, **13**, 461–482, doi:10.5194/gmd-13-461-2020.
- 447 Gauss, M., Myhre, G., Isaksen, S.A., et al. 2006. Radiative forcing since preindustrial times due to  
448 ozone change in the troposphere and the lower stratosphere. *Atmospheric Chemistry and Physics*, **6**,  
449 575–599, doi: 10.5194/acp-6-575-2006.
- 450 Heue, K.P., Cold-Egbers, M., Delcloo, A., et al. 2016. Trends of tropical tropospheric ozone from 20  
451 years of European satellite measurements and perspectives for the Sentinel-5 Precursor.  
452 *Atmospheric Measurement Techniques*, **9**, 5037–5051, doi: 10.5194/amt-9-5037-2016.
- 453 Hurtmans, D., Coheur, P.-F., Wespes, C., et al. 2012. FORLI radiative transfer and retrieval code for  
454 IASI, *Journal of Quantitative Spectroscopy and Radiative Transfer*, **113**, 1391–1408,  
455 doi:10.1016/j.jqsrt.2012.02.036. Iglesias-Suarez, F., Kinnison, D.E., Rap, A., et al. 2018. Key drivers of  
456 ozone change and its radiative forcing over the 21<sup>st</sup> century. *Atmospheric Chemistry and Physics*, **18**,  
457 6121–6139, doi:10.5194/acp-18-6121-2018.
- 458 IASI-IMS. 2022. IASI-IMS Data [Dataset],  
459 [https://homepages.see.leeds.ac.uk/~earrijo/to3re/iasi\\_ims/](https://homepages.see.leeds.ac.uk/~earrijo/to3re/iasi_ims/) (last accessed 01/01/2023).
- 460 IASI-FORLI. 2020. Daily IASI/Metop-A ULB-LATMOS ozone (O3) L2 product (total column and  
461 vertical profile) (v20151001) [Dataset], <https://iasi.aeris-data.fr/catalog/> (last accessed  
462 15/12/2022).



- 463 IASI-SOFRID. 2022. Welcome to the IASI-SOFRID database (vn3.5) [Dataset],  
464 <http://thredds.sedoo.fr/iasi-sofrid-o3-co/> (last accessed 01/12/2022).
- 465 Iglesias-Suarez, F., Kinnison, D.E., Rap, A., et al. 2018. Key drivers of ozone change and its radiative  
466 forcing over the 21st century. *Atmospheric Chemistry and Physics*, **18**(9), 6121-6139, doi:  
467 10.5194/acp-18-6121-2018.
- 468 oiner, J., Schoeberl, R.M., Vasilkov, A.P., et al. 2009. Accurate satellite-derived estimates of the  
469 tropospheric ozone impact on the global radiation budget. *Atmospheric Chemistry and Physics*, **9**,  
470 4447-4465, doi: 10.5194/acp-9-4447-2009.
- 471 Keppins, A., Lambert, J.C., Granville, J., et al. 2018. Quality assessment of the Ozone\_cci Climate  
472 Research Data Package (release 2017) – Part 2: Ground-based validation of nadir ozone profile data  
473 products. *Atmospheric Measurement Techniques*, **11**, 3769-3800, doi: 10.5194/amt-11-3769-2018.
- 474 Lamarque, J.F., Bond, T.C., Eyring, V., et al. 2010. Historical (1850-2000) gridded anthropogenic and  
475 biomass burning emissions of reactive gases and aerosols: methodology and application.  
476 *Atmospheric Chemistry and Physics*, **10**, 7017-7039, doi: 10.5194/acp-10-7017-2010.
- 477 Mann, G.W., Carslaw, K.S., Spracklen, D.V., et al. 2010. Description and evaluation of GLOMAP-  
478 mode: A modal global aerosol microphysics model for the UKCA composition-climate  
479 model. *Geoscientific Model Development*, **3**(2), 519– 551, doi:10.5194/gmd-3-519-2010.
- 480 McPeters, R.D., Labow, G.J., and Logan, J.A. 2007. Ozone climatological profiles for satellite retrieval  
481 algorithms. *Journal of Geophysical Research*, **112** (D05308), <https://doi.org/10.1029/2005JD006823>.
- 482 Monks, S.A., Arnold, S.R., Hollaway, M.J., et al. 2017. The TOMCAT global chemistry transport model  
483 v1.6: Description of chemical mechanism and model evaluation. *Geoscientific Model  
484 Development*, **10**(8), 3025– 3057, doi:0.5194/gmd-10-3025-2017.
- 485 Morgenstern, O., Hegglin, M.I., Rozanov, E., et al. 2017. Review of the global models used with phase  
486 1 of the Chemistry-Climate Model Initiative (CCMI). *Geoscientific Model  
487 Development*, **10**(2), 639– 671, doi:10.5194/gmd-10-639-2017.
- 488 Moxy, W.J. and Levy, H. 2000. A model analysis of tropical South Atlantic Ocean tropospheric ozone  
489 maximum: The interaction of transport and chemistry. *Journal of Geophysical Research*, **105** (D13),  
490 17393-17415, doi:10.1029/2000JD900175.
- 491 Myhre, G., Shindell, D., Breon, F.M., et al. 2013. Anthropogenic and Natural Radiative Forcing, in:  
492 Climate Change 2013: The Physical Science Basis. Contribution of Working Group I to the Fifth  
493 Assessment Report of the Intergovernmental Panel on Climate Change Cambridge University Press,  
494 Cambridge, United Kingdom and New York, NY, USA, 659–740.
- 495 Nassar, R., Logan, J.A., Mergretskaja, I.A., et al. 2009. Analysis of tropical tropospheric ozone, carbon  
496 monoxide, and water vapor during the 2006 El Niño using TES observations and the GEOS-Chem  
497 model. *Journal of Geophysical Research: Atmospheres*, **114** (D17304), doi: 10.1029/2009JD011760.
- 498 NOAA. 2023. ESRL/GML Ozonesondes [Dataset], <https://gml.noaa.gov/ozwv/ozsondes/> (last  
499 accessed 01/06/2022).
- 500 Olivier, J., Peters, J., Granier, C., et al. 2003. Present and future surface emissions for atmospheric  
501 compounds, *POET report #2*, Available at: [http://accent.aero.jussieu.fr/Documents/del2\\_final.doc](http://accent.aero.jussieu.fr/Documents/del2_final.doc)  
502 (last accessed 23/01/2023).
- 503 Pacifico, F., Harrison, S.P., Jones, C.D., et al. 2011. Evaluation of a photosynthesis-based biogenic  
504 isoprene emission scheme in JULES and simulation of isoprene emissions under present-day climate  
505 conditions, *Atmospheric Chemistry and Physics*, **11**, 4371–4389, doi:10.5194/acp-11-4371-2011.



- 506 Pimlott, M.A., Pope, R.P., Kerridge, B.J., et al. 2022. Investigating the global OH radical distribution  
507 using steady-state approximations and satellite data. *Atmospheric Chemistry and Physics*, **22**, 10467-  
508 10488, doi: 10.5194/acp-22-10467-2022.
- 509 Rap, A., Richard, N.A.D., Forster, P.M., et al. 2015. Satellite constraint on the tropospheric ozone  
510 radiative effect. *Geophysical Research Letters*, **42**, 5074–5081, doi: 10.1002/2015GL064037.
- 511 Richards, N.A.D, Osterman, G.B., Browell, E.V., et al. 2008. Validation of tropospheric emission  
512 spectrometer ozone profiles with aircraft observations during the intercontinental chemical  
513 transport experiment–B. *Journal Geophysical Research*, **113**(D16S29), doi: 10.1029/2007JD008815.
- 514 Rodgers, C.D. 2000. Inverse methods for atmospheric sounding: Theory and practice. New Jersey,  
515 USA: World Science.
- 516 Rowlinson, M.J., Rap, A., Hamilton, D.S., et al. 2020. Tropospheric ozone radiative forcing uncertainty  
517 due to pre-industrial fire and biogenic emissions. *Atmospheric Chemistry and Physics*, **20**, 10937-  
518 10951, doi: 10.5194/acp-20-10937-2020.
- 519 Saunders, R., Matricardi, M., and Brunel, P. 1999. An improved fast radiative transfer model for  
520 assimilation of satellite radiance observations. *Quarterly Journal of the Royal Meteorological Society*,  
521 **125** (556 part B), 1407–1425, doi:10.1256/smsqj.55614.
- 522 Scott, C.E., Monks, S.A., Spracklen, D.V., et al. 2018. Impact on short-lived climate forcers increases  
523 projected warming due to deforestation. *Nature Communications*, **9**, 157, doi: 10.1038/s41467-017-  
524 02412-4.
- 525 Sellar, A.A., Jones, C.G., Mulcahy, J.P., et al. 2019. Description and Evaluation of the UK Earth System  
526 Model. *Journal of Advances in Modeling Earth Systems*, **11**, 4513-4558, doi:  
527 10.1029/2019MS001739.
- 528 SHADOZ. 2023. SHADOZ Data Archive [Dataset], <https://tropo.gsfc.nasa.gov/shadoz/Archive.html>  
529 (last accessed 01/06/2022).
- 530 Sitch, S., Cox, P.M., Collins, W.J., et al. 2007. Indirect radiative forcing of climate change through  
531 ozone effects on the land-carbon sink. *Nature*, **448**, 791-794, doi: 10.1038/nature06059.
- 532 Sofieva, V.F., Tamminen, J., Kyrölä, E., et al. 2014. A novel tropopause-related climatology of ozone  
533 profiles. *Atmospheric Chemistry and Physics*, **14**, 283–299, doi:10.5194/acp-14-283-2014.
- 534 Stevenson, D.S., Young, P.J., Naik, V., et al. 2013. Tropospheric ozone changes, radiative forcing and  
535 attribution to emissions in the Atmospheric Chemistry and Climate Model Intercomparison Project  
536 (ACCMIP), *Atmospheric Chemistry and Physics*, **13**, 3063- 3085, doi: 10.5194/acp-13-3063-2013.
- 537 TOMCAT. 2023. TOMCAT Simulations [Dataset],  
538 <https://homepages.see.leeds.ac.uk/~earrjpo/to3re/tomcat/> (last accessed 23/01/2023).
- 539 van der Werf, G. R., Randerson, J. T., Giglio, L., et al. 2017. Global fire emissions estimates during  
540 1997–2016. *Earth System Science Data*, **9**, 697–720, doi:10.5194/essd-9-697-2017.
- 541 Wespes, C., Hurtmans, D., Clerbaux, C., Boynard, A., and Coheur, P.-F.: Decrease in tropospheric O<sub>3</sub>  
542 levels in the Northern Hemisphere observed by IASI, *Atmos. Chem. Phys.*, **18**, 6867–6885,  
543 <https://doi.org/10.5194/acp-18-6867-2018>, 2018.
- 544 Worden, H.M., Bowman, K.W., Worden, J.R., et al. 2008. Satellite measurements of the clear-sky  
545 greenhouse effect from tropospheric ozone. *Nature Geoscience*, **1**, 305-308, doi:  
546 [doi.org/10.1038/ngeo182](https://doi.org/10.1038/ngeo182).



547 Worden, H.M., Bowman, K.W., Kulawik, S.S., et al. 2011. Sensitivity of outgoing longwave radiative  
548 flux to the global vertical distribution of ozone characterized by instantaneous radiative kernels from  
549 Aura-TES. *Journal of Geophysical Research: Atmospheres*, 116 (D14115), doi:10.1029/2010JD015101.

550 WOUDC. 2023. Data Search/Download [Dataset], <https://woudc.org/data/explore.php> (last accessed  
551 01/06/2022).

552 Young, P.J., Archibald, A.T., Bowman, K.W., et al. 2013. Pre-industrial to end 21st century projections  
553 of tropospheric ozone from the Atmospheric Chemistry and Climate Model Intercomparison Project  
554 (ACCMIP). *Atmospheric Chemistry and Physics*, **13**, 2063-2090, doi: 10.5194/acp-13-2063-2013.

555

556

557

558

559

560

561

562

563

564

565

566

567

568

569

570

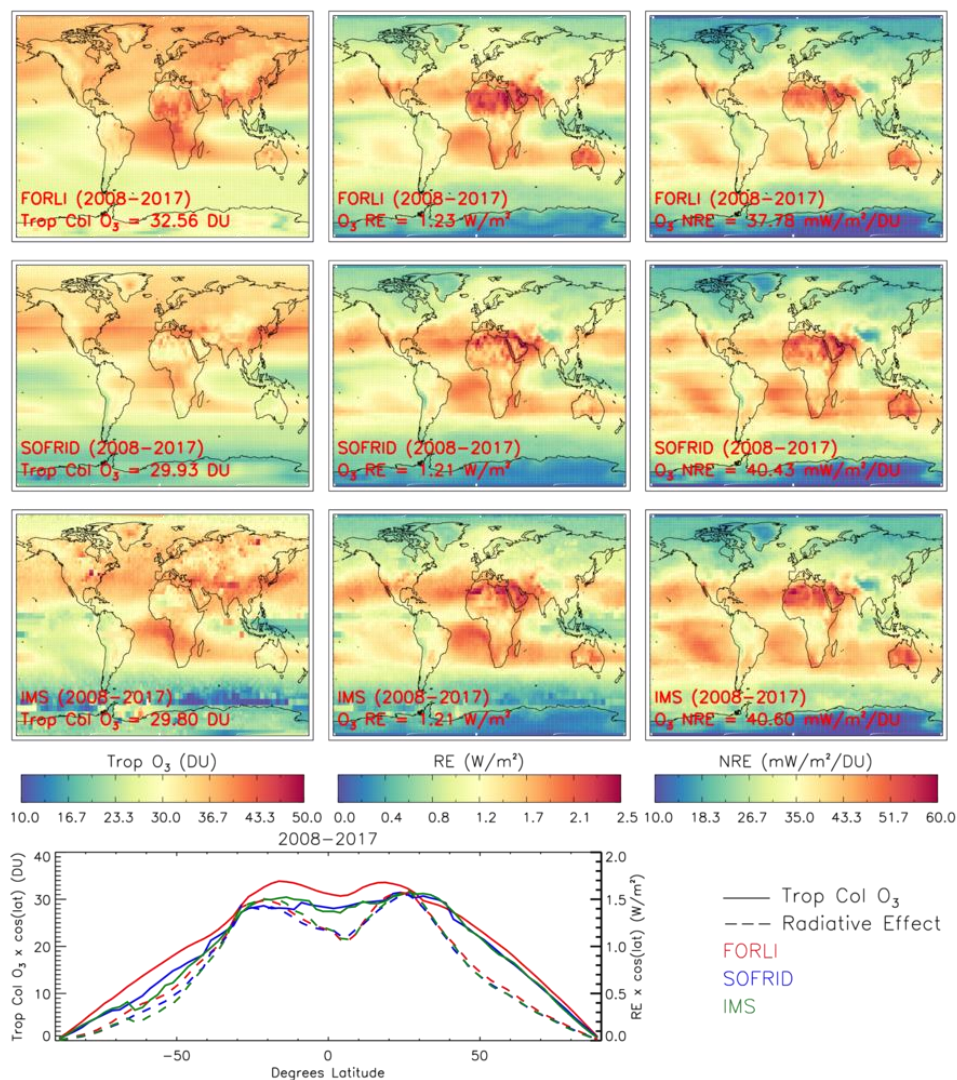
571

572

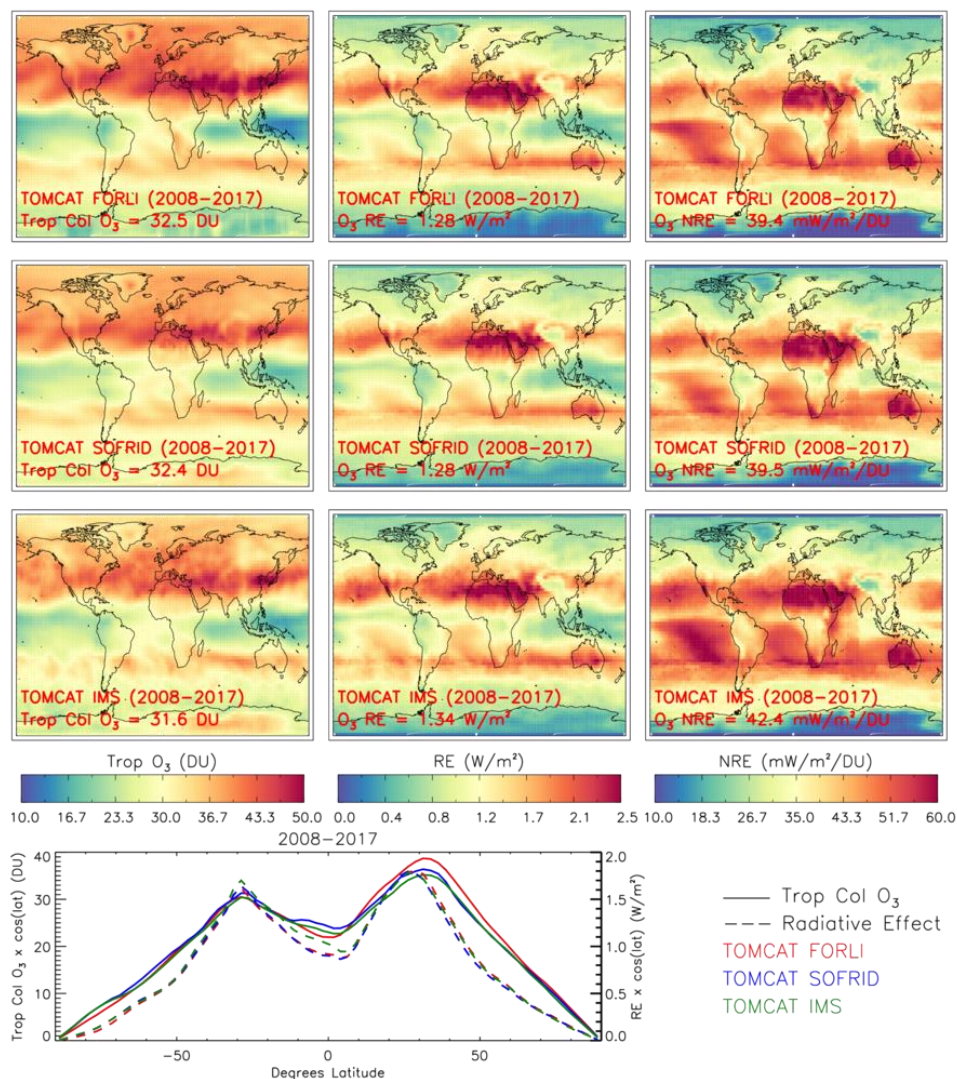
573



574 **Figures:**



575  
 576 **Figure 1:** Tropospheric column O<sub>3</sub> (TCO<sub>3</sub>, DU), tropospheric O<sub>3</sub> radiative effect (TO<sub>3</sub>RE, W/m<sup>2</sup>) and  
 577 normalised TO<sub>3</sub>RE (NTO<sub>3</sub>RE, mW/m<sup>2</sup>/DU) averaged for 2008 to 2017 for IASI-FORLI (top row), IASI-  
 578 SOFRID (middle row) and IASI-IMS (bottom row). Zonal averages of TCO<sub>3</sub> (DU, solid lines) and TO<sub>3</sub>RE  
 579 (W/m<sup>2</sup>, dashed lines), both weighted by cosine of latitude, is shown in the bottom panel from all the  
 580 IASI instruments.



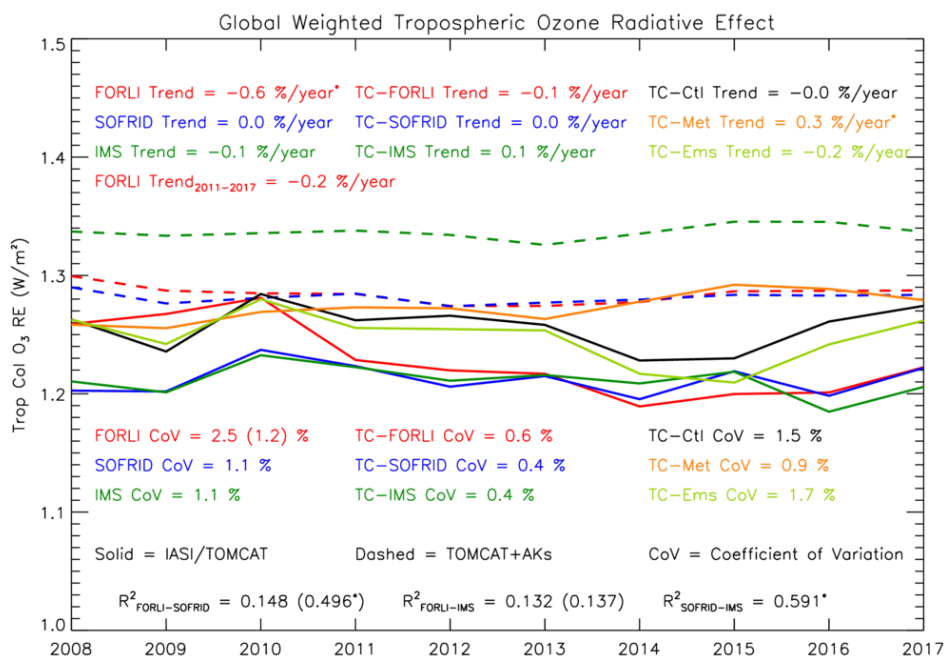
581  
 582 **Figure 2:** TCO<sub>3</sub> (DU), TO<sub>3</sub>RE (W/m<sup>2</sup>) and NTO<sub>3</sub>RE (mW/m<sup>2</sup>/DU) averaged for 2008 to 2017 for  
 583 TOMCAT with the averaging kernels (AKs) applied from IASI-FORLI (top row), IASI-SOFRID (middle  
 584 row) and IASI-IMS (bottom row). Zonal averages of TCO<sub>3</sub> (DU, solid lines) and TO<sub>3</sub>RE (W/m<sup>2</sup>, dashed  
 585 lines), both weighted by cosine of latitude, is shown in the bottom panel from all the IASI  
 586 instruments.

587

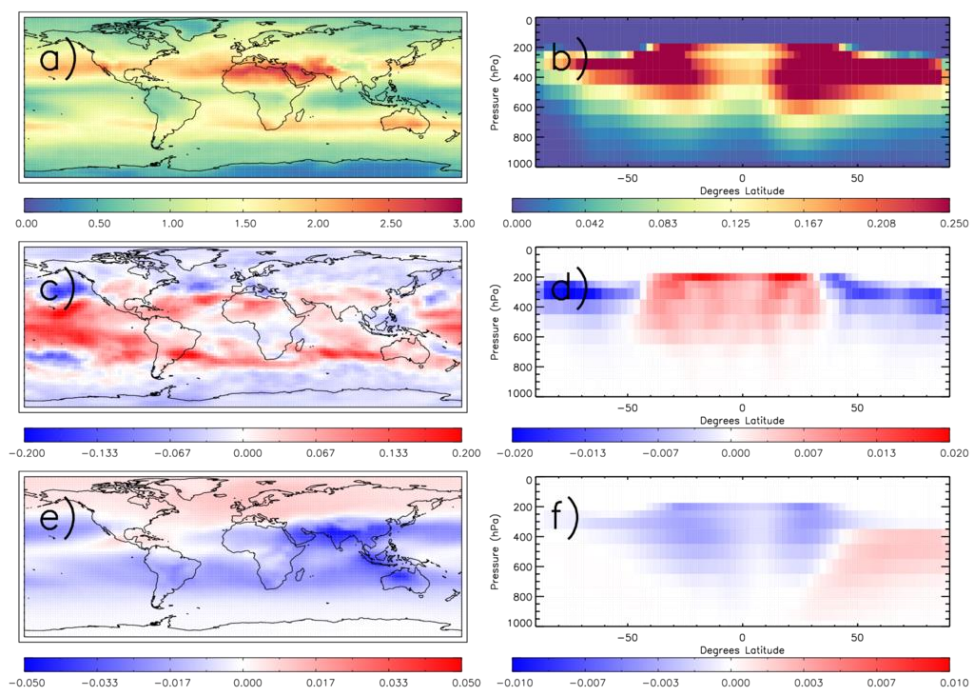
588

589





590  
 591 **Figure 3:** Annual global mean time-series of  $TO_3RE$  ( $W/m^2$ ), between 2008 and 2017, for IASI-FORLI  
 592 (red-solid), IASI-SOFRID (blue-solid) and IASI-IMS (green-solid). TOMCAT with the IASI-FORLI (red-  
 593 dashed), IASI-SOFRID (blue-dashed) and IASI-IMS (green-dashed) AKs applied, original TOMCAT  
 594 simulation (black-solid), TOMCAT with fixed emissions (lime-solid) and TOMCAT with fixed  
 595 meteorology (orange-solid) are also shown. The linear trend (%/year) is shown as well as the  
 596 percentage coefficient of variation (CoV). The correlation between IASI time-series are shown by the  
 597  $R^2$  values. Significant linear trends and correlations in the  $TO_3RE$  are shown by an \*. TC represents  
 598 TOMCAT. The IASI-FORLI trend for 2011 to 2017 is also shown as well as the CoV and  $R^2$  in brackets in  
 599 addition to the statistical metrics over the full time period due to record inhomogeneities prior to  
 600 2011 (Boynard et al., 2018).



601

602 **Figure 4:** a) TOMCAT control run TO<sub>3</sub>RE (W/m<sup>2</sup>), b) TOMCAT control run zonal average grid box O<sub>3</sub>  
603 radiative effect (W/m<sup>2</sup>), c) TOMCAT fixed meteorology – TOMCAT control TO<sub>3</sub>RE difference (W/m<sup>2</sup>),  
604 d) TOMCAT fixed meteorology – TOMCAT control zonal average grid box O<sub>3</sub> radiative effect  
605 difference (W/m<sup>2</sup>), e) TOMCAT fixed emissions – TOMCAT control TO<sub>3</sub>RE difference (W/m<sup>2</sup>), f)  
606 TOMCAT fixed emissions – TOMCAT control zonal average grid box O<sub>3</sub> radiative effect difference  
607 (W/m<sup>2</sup>).

608